



Ultra-low Pt-loaded catalyst based on nickel mesh for boosting alkaline water electrolysis

Junyu Zhang¹, Jian Dang¹, Xiaohong Zhu, Jugang Ma^{*}, Mingguo Ouyang, Fuyuan Yang^{*}

School of Vehicle and Mobility, Tsinghua University, Beijing, China

ARTICLE INFO

Keywords:

Electrocatalyst
Hydrogen evolution reaction
Oxygen evolution reaction
Alkaline water electrolysis
Low cost of hydrogen production

ABSTRACT

Green hydrogen produced by water electrolysis is an important form of energy storage for centralized, large-scale and long-cycle scenarios. Cost efficiency is crucial in promoting this green energy storage approach; hence, developing a low-cost and efficient catalyst for water electrolysis is essential. This study describes a method to improve the catalytic activity of nickel wire mesh by using ultra-low Pt (0.06 mg cm^{-2}) doped $\text{Ni}(\text{OH})_2$ arrays, which improves the charge kinetics, active surface area and intrinsic activity of the active sites. The target electrode requires only 68 and 269 mV @ 100 mA cm^{-2} for the hydrogen evolution reaction (HER) and oxygen evolution reaction (OER), respectively, in alkaline electrolyte. The two-electrode water-splitting system assembled by the proposed electrode outperformed the noble-metal pair $\text{Pt/C@NM} \parallel \text{RuO}_2 \text{ @NM}$. The performance of the assembled alkaline water electrolyzer is also outstanding (required only 1.87 V to reach 400 mA cm^{-2}) with excellent durability (> 600 h).

1. Introduction

The exploration and research on new energy are imminent because the current conflicts between countries in the world has exacerbated the energy crisis, and people in many countries are facing severe challenges from energy shortage [1,2]. The research on solar, wind and other environmentally friendly energy sources is burgeoning [3–6]. However, external factors, such as seasonality, regionality, and volatility, significantly limit the use of these energy sources [7–9]. Conversely, hydrogen has an extremely broad application potential as a secondary storage energy source because of its availability from a wide variety of sources, high calorific value, and non-polluting nature [10–12].

The water-splitting reaction is the ideal method to produce green hydrogen. The International Energy Agency predicts that the global hydrogen demand will reach 120 Mt in 2025 and approximately 520 Mt in 2050 [13]. However, the high price of hydrogen production limits its application (which is approximately 4.90–10.40 \$ kg^{-1} today with an electricity cost of 53 \$ MWh^{-1}) [14,15]. The electrolyzer is a major contributor to the hydrogen production cost (approximately 770 \$ MW^{-1}). The future goal is to reduce this cost by 80% to 130 \$ MW^{-1} [15]. Hence, it is important to develop an efficient energy conversion/storage device [16,17]. The water-splitting reaction consists of

two half-reactions: hydrogen evolution reaction (HER) and oxygen evolution reaction (OER) [18,19]. However, HER and OER require high energy to drive the reaction and this results in slower kinetics [20]. Noble metals (Pt, Ru and Ir) have proven to be ideal catalysts for HER and OER, but the excessive price limits their wide application [21].

Nickel foam (NF), with a unique three-dimensional structure and net-like channels, can effectively promote charge transport and act as a substrate to construct various microstructures. However, its low toughness and loosely attached electroactive components greatly limit its practical application [22]. Conversely, nickel mesh (NM) is widely used in practical electrolyzers because of its excellent mechanical strength and stability, however, its lower surface area often results in a larger overpotential [23]. Transition metal hydroxides (TMH) are potential alternatives to noble metal catalysts due to their abundant reserves, easy synthesis method, high theoretical activity and stability [24]. Nickel hydroxide, in particular, has been widely studied as a catalyst for alkaline water electrolysis because of its stability and high catalytic activity in alkaline environments [25]. For example, Wu et al. reported a $\text{Ni}(\text{OH})_2$ catalyst based on NF that exhibited OER and HER activities higher than those of NF (NF : $\eta_{10} \approx 0.4 \text{ V}$, Tafel slope = 138 mV dec^{-1} for HER; $\eta_{10} \approx 1.63 \text{ V}$, Tafel slope = 136 mV dec^{-1} for OER. $\text{Ni}(\text{OH})_2/\text{NF}$: $\eta_{10} \approx 0.27 \text{ V}$, Tafel slope = 140 mV dec^{-1} for HER; $\eta_{10} \approx$

^{*} Corresponding authors.

E-mail addresses: majugang2015@qq.com (J. Ma), fyyang@tsinghua.edu.cn (F. Yang).

¹ These authors contributed equally to this work

1.57 V, Tafel slope = 110 mV dec⁻¹ for OER) [26]. This improved catalytic performance is mainly attributed to the design of the nanostructures and the increase in geometric area, which enhances the charge transport rate and the electrochemical active area of the catalyst.

Although many TMH catalysts have shown promising results, their performance still falls short compared to the noble metal catalysts because of the low exposure of active sites and poor intrinsic activity [27]. Interface engineering and elemental doping are typical methods for improving the HER/OER activity by modulating the d-orbital and spin states of catalyst [28,29]. These modifications can alter the Gibbs adsorption energy and charge environment, thus improving the overall catalytic activity [30,31]. Proper noble metal doping is a proven strategy to substantially enhance the HER and OER activities of catalysts and increase their energy efficiency [32]. Furthermore, theoretical and experimental results show that Pt has good adsorption capacity for both hydrogen-containing and oxygen-containing intermediates [33]. However, trace doping of Pt does not significantly increase the cost, but it substantially enhances the utilization of noble metals [34]. For example, Zhou et al. synthesized Pt-doped NiO/Ni heterostructures on Ag NWs as catalysts for HER, which outperformed commercial Pt/C (η_{10} = 26 mV, η_{100} = 85 mV, Tafel slope = 27 mV dec⁻¹) [35]. However, most Pt-based nanocatalysts are in powder form. They require Nafion to adhere to the catalyst, which leads to the loss of electrode conductivity and active sites, and the poor cohesive strength of Nafion easily leads to Pt shedding.

Based on these considerations, we synthesized a series of Pt-doped Ni(OH)₂ catalysts based on NF and NM. After comparing their catalytic performances, we selected the Pt-Ni(OH)₂@NM for investigation owing to its potential for applications. The Pt-Ni(OH)₂@NM catalyst is produced by homogeneously dispersing Pt nanoparticles with an average size of 3.1 nm on a Ni(OH)₂ nanowire/nanosheet composite structure. The composite structure was obtained by applying the hydrothermal method on a NM substrate, followed by the electrodeposition of Pt nanoparticles. This smart design has several advantages for electrocatalysis. First, ultrafine and homogeneous Pt nanoparticles can increase the electrochemically active area, which may enhance the adsorption and activation of reactants. Second, the synergistic interaction between Pt and Ni(OH)₂ modifies the electronic binding energies of Pt and Ni, optimizing their interactions with reaction intermediates, which can result in improved electrocatalytic kinetics. Third, the NM support has excellent resistance to corrosion and a high charge transfer rate in an alkaline environment, and the in-situ integration contributes to strong adhesion between the support and the hybrid catalyst. Additionally, the material cost of this electrode is only 0.002 \$ cm⁻² higher than NM. The as-prepared Pt-Ni(OH)₂@NM electrode exhibits low overpotentials of 68 and 269 mV to achieve HER and OER current densities of 100 mA cm⁻², respectively, in a 1 M KOH solution. When the Pt-Ni(OH)₂@NM electrode is used to assemble a two-electrode water-splitting system, it requires only 1.491 V to achieve 10 mA cm⁻², beating the noble metal pair Pt/C@NM || RuO₂@NM. Additionally, when Pt-Ni(OH)₂@NM electrode is used to assemble an alkaline water electrolyzer, it only needs 1.87 V to reach 400 mA cm⁻² at 80 °C and works steadily for more than 600 h. These results demonstrate the outstanding electrocatalytic activity and long-term operational lifespan of a Pt-doped Ni(OH)₂ electrode for water electrolysis.

2. Experimental

2.1. Preparation of Ni(OH)₂@NM

The NM (3 × 3 cm²) was first ultrasonically pretreated with acetone, ethanol, 3 M HCl (M.W. 36.46, Beijing Tongguang Fine Chemical Company) and deionized water sequentially for 20 min, and dried in a vacuum oven at 60 °C for 12 h for further use.

Then, the green solution is achieved by dissolving 2 mmol NiCl₂ (Anhydrous, Ni > 42%, Adamas-beta) and 9 mmol urea (99.0%, BeiJing

Chemical Works) in 100 mL deionized water and stirring magnetically for 20 min. Next, the solution was poured into a 100 mL Teflon liner, and a clean piece of NM was dipped into the solution (the top surface of the NM was covered with Teflon tape to avoid the effect of by-product deposition during the reaction). Afterward, the reactor was maintained at 120 °C for 6 h and cooled naturally to room temperature. Finally, the NM was removed, rinsed several times with deionized water and alcohol, and dried in a vacuum oven at 80 °C for 12 h to obtain Ni(OH)₂@NM.

2.2. Preparation of Pt doped Ni(OH)₂@NM (Pt-Ni(OH)₂@NM)

The target sample, Pt-Ni(OH)₂@NM, was prepared via electrodeposition. A three-electrode system was assembled in which Ni(OH)₂@NM was used as the working electrode, a Hg|HgO electrode as the reference electrode, and a carbon rod as the counter electrode. The electrochemical process was achieved by multiple CV process in 1 M KOH electrolyte containing 20 μM H₂PtCl₆·6 H₂O (Pt 37.5%, Aladdin) with a scan rate of 50 mV s⁻¹ of 0 to -0.5 V vs. RHE for 50 cycles.

The Ni(OH)₂@NM was replaced with NM, and the sample prepared by electrodeposition of Pt using the same method was named Pt@NM.

2.3. Preparation of Ni(OH)₂@NF, Pt doped Ni(OH)₂@NF (Pt-Ni(OH)₂@NF) and Pt@NF

Ni(OH)₂@NF, Pt-Ni(OH)₂@NF and Pt@NF were prepared using the same method stated in Section 2.2, replacing NM with NF. The mass loading of each catalyst was ~ 2.5 mg cm⁻².

2.4. Preparation of Pt/C@NF and RuO₂@NF

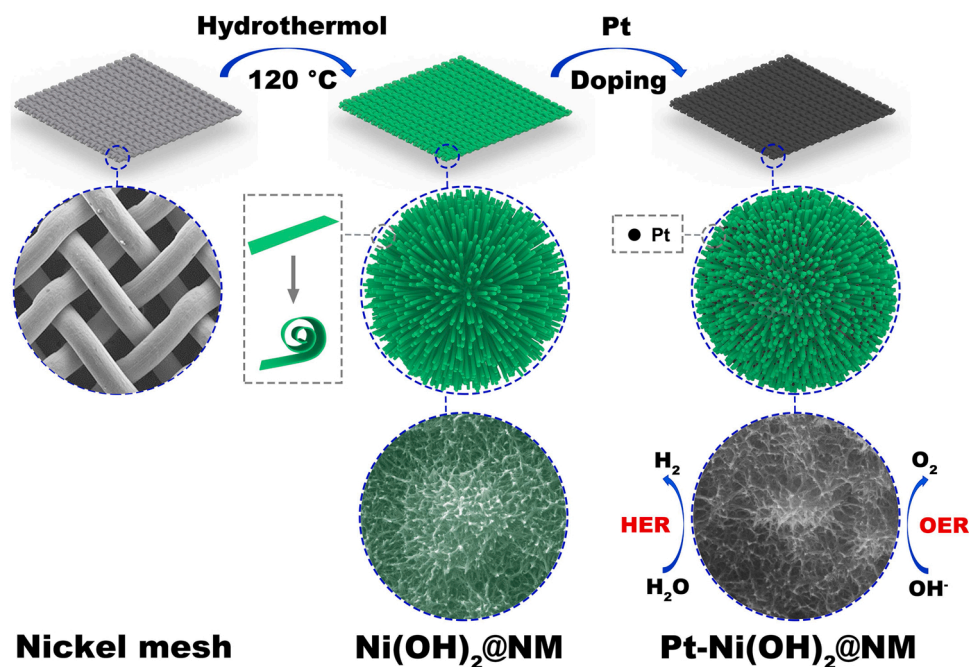
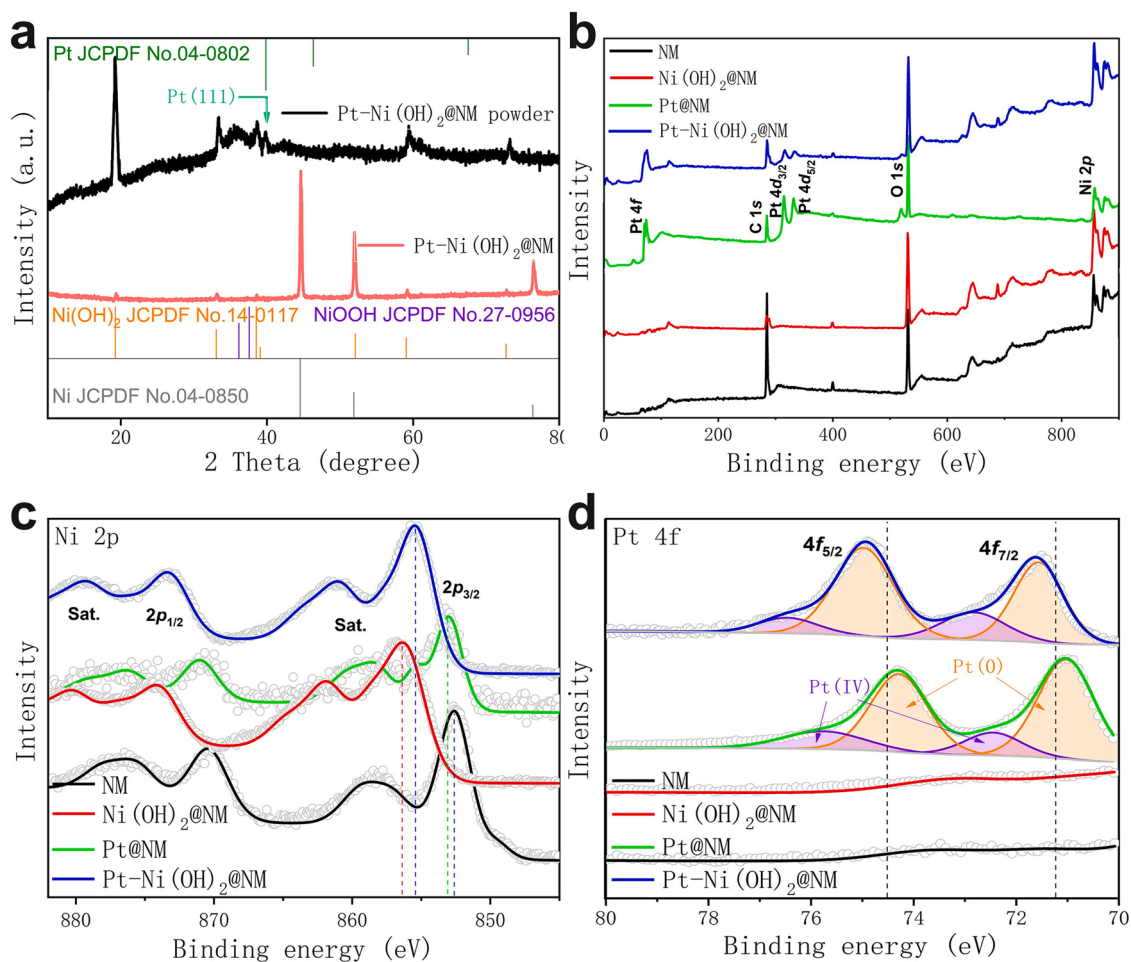
10 mg 20% Pt/C (M.W. 195.08, Pt 20%, Macklin) or RuO₂ (M.W. 133.07, 99.9%, Macklin) was dispersed in 330 μL of water / ethanol / 5 wt% Nafion (V / V / V = 150: 150: 30) and sonicated for at least 20 min. Then 10 μL of the catalyst ink was pipetted onto the NM with a mass loading of approximately 2.5 mg cm⁻².

3. Results and discussion

3.1. Synthesis and characterizations of Pt-Ni(OH)₂@NM

The target NM-based catalyst Pt-Ni(OH)₂@NM nanowire/nanosheet composite structure was obtained using a two-step method, as shown in Fig. 1 and detailed in the experimental section. First, Ni(OH)₂ nanowire/nanosheet arrays were grown on the NM surface using a hydrothermal method. The nanowire structure was formed by the convolution of the nanosheet. This nanowire/nanosheet composite structure is explained in detail in the Scanning electron microscopy (SEM) and Transmission electron microscopy (TEM) sections. The target catalyst Pt-Ni(OH)₂@NM was then obtained by electrodeposition. Pt-Ni(OH)₂@NM has a large geometric area and high conductivity based on the NM substrate, which ensures the rapid transfer of charge and gas products (H₂ and O₂) and sufficient contact between the catalyst surface and electrolyte.

Next, the crystal structure of each sample was obtained using X-ray diffraction (XRD). From Fig. S1, it can be seen that Ni(OH)₂@NM exhibits distinct peaks at 19.3°, 33.1°, 38.5° and 59.1°, which correspond to Ni(OH)₂ (JCPDF No. 14-0117). The relative height of the characteristic peak of Ni(OH)₂@NF is much lower, indicating its poor crystallinity. After Pt doping, no significant peak was observed for either Pt@NM or Pt@NF, which may be owing to the low Pt content and interference of the NM and NF substrates. Pt-Ni(OH)₂@NM and Pt-Ni(OH)₂@NF demonstrated phase information similar to Ni(OH)₂@NM, Ni(OH)₂@NF. Since Pt-Ni(OH)₂@NM was the focus of this work, we scraped off the catalyst powder to avoid the interference of NM and analyzed its XRD spectrum (Fig. 2a). The characteristic peak corresponds almost identically to the standard peak of Ni(OH)₂ when the

Fig. 1. Schematic illustration of Pt-Ni(OH)₂@NM.Fig. 2. a, XRD spectrum of Pt-Ni(OH)₂@NM. XPS spectra for NM, Ni(OH)₂@NM, Pt@NM and Pt-Ni(OH)₂@NM: b, Full scan spectra; c, Ni 2p spectra, dashed lines represent the 2p_{3/2} peak of each catalyst; d, Pt 4f spectra, dashed lines represent 4f_{5/2} and 4f_{7/2} peaks of Pt foil [41,42].

disturbance from NM is absent. A weaker diffraction signal at 39.8° corresponding to the (111) crystal plane of Pt (JCPDF No. 04-0802) is also observable, which proves the successful doping of Pt^0 . A broad peak appears at 36° , corresponding to the (101) crystal plane of NiOOH (JCPDF No. 27-0956), which is formed by incomplete dehydration of $\text{Ni}(\text{OH})_2$ during hydrothermal reaction.

Furthermore, the elemental composition and valence states of the sample were analyzed using X-ray photoelectron spectroscopy (XPS). The XPS spectra in Fig. 2b confirms the presence of Pt, Ni and O in Pt-Ni(OH)₂@NM. The quantitative percentages of each element in the samples are presented in Table S1. Although Pt@NM and Pt-Ni(OH)₂@NM electrodeposited Pt in the same way, it is clear that the $\text{Ni}(\text{OH})_2$ precursor caused more Pt to be deposited on the surface of the sample. Fig. 2c compares the Ni 2p spectra of NM, $\text{Ni}(\text{OH})_2$ @NM, Pt@NM and Pt-Ni(OH)₂@NM. The Ni 2p_{3/2} of Pt@NM (853.1 eV) increases by 0.4 eV compared to NM (852.7 eV). This is due to the lower electronegativity of Ni (1.92 EN) than that of Pt (2.28 EN). The lower electronegativity causes electrons to transfer to Pt, resulting in a larger electron binding energy of Pt@NM. Ni 2p_{3/2} in $\text{Ni}(\text{OH})_2$ @NM is located at 856.4 eV, corresponding to the $\text{Ni}^{2+}/\text{Ni}^{3+}$ of $\text{Ni}(\text{OH})_2/\text{NiOOH}$ [36,37]. After Pt doping, the Ni 2p_{3/2} peak of Pt-Ni(OH)₂@NM undergoes a negative shift (855.5 eV). This is because the charge in $\text{Ni}(\text{OH})_2$ is transferred to O, which has a larger electronegativity (3.44 EN) than Pt. This tendency is favorable for regulating the charge environment on the catalyst surface, thus modulating the catalyst activity, which was confirmed by previous reports [38,39]. Fig. 2d compares the Pt 4f high-resolution spectra of the samples. Pt is detected only on the Pt@NM and Pt-Ni(OH)₂@NM surfaces, proving its successful deposition. The peaks of both Pt@NM and Pt-Ni(OH)₂@NM consist of two valence states, Pt^0 and Pt^{4+} , where Pt^{4+} is caused by the adsorption of PtCl_6^{2-} ions on the sample surface during the preparation process [40]. The two dashed lines at 71.2 eV and 74.5 eV match the characteristic peaks of Pt^0 4f_{7/2} and 4f_{5/2}, respectively [41,42]. Pt^0 4f_{7/2} (70.9 eV) for Pt@NM decreases by 0.3 eV compared to the standard Pt^0 4f_{7/2}

(71.2 eV), while Pt^0 4f_{7/2} (71.6 eV) for Pt-Ni(OH)₂@NM increases by 0.4 eV compared to the standard Pt^0 4f_{7/2}. The change of binding energy for Ni 2p and Pt 4f reflects the construction of the Pt-substrate synergistic system [43], which can regulate the electronic energy states on the catalyst surface, affecting adsorption free energy and charge transport kinetics.

The microscopic morphologies of the catalysts were analyzed by SEM, Fig. S2 and Fig. S3 show the morphologies of the samples based on the NF and NM substrates, respectively (NF, $\text{Ni}(\text{OH})_2$ @NF, Pt@NF and Pt-Ni(OH)₂@NF; NM, $\text{Ni}(\text{OH})_2@NM, Pt@NM and Pt-Ni(OH)₂@NM). The samples grown on both substrates exhibit the same morphology, but the NM substrate has better conductivity than the NF substrate, because NM substrate shows better resolution at the same magnification as the NF substrate. The grown $\text{Ni}(\text{OH})_2$ appears to be a dense and uniform array of nanowires with a < 10 nm width. Pt is deposited directly on the substrates (Pt@NF and Pt@NM), and stacked to form particles with a diameter of approximately 30 nm. The microscopic morphologies of Pt-Ni(OH)₂@NF and Pt-Ni(OH)₂@NM are consistent with those of $\text{Ni}(\text{OH})_2$ @NF and $\text{Ni}(\text{OH})_2@NM. Pt deposited on the surface of $\text{Ni}(\text{OH})_2$ could not be directly observed at the 100 nm scale (Fig. 3a). The finer the Pt particles, the larger the dispersion area, the lower the cost, and the higher the utilization of noble metals. The BET test results demonstrated that the initial surface area of NM is much smaller than that of NF (approximately 38.5% of NF). After the growth of $\text{Ni}(\text{OH})_2$, the surface areas of Pt-Ni(OH)₂@NM is comparable to that of Pt-Ni(OH)₂@NF (approximately 75.2% of the later) (Table S2).$$

The internal structure of the samples was further observed by TEM. Fig. S4 shows SEM and TEM images of Pt-Ni(OH)₂@NF and Pt-Ni(OH)₂@NM. Only the nanowire array can be seen in Fig. S4a and d, but after ultrasonic stripping of the sample from the substrate, many nanosheet fragments can be observed in the TEM images (Fig. S4b and e). At higher magnifications, it can be seen that nanowires appear at the edges of nanosheets, formed by their convolution, which has a larger area and increased activity [44]. The nanowires in Pt-Ni(OH)₂@NF are thicker,

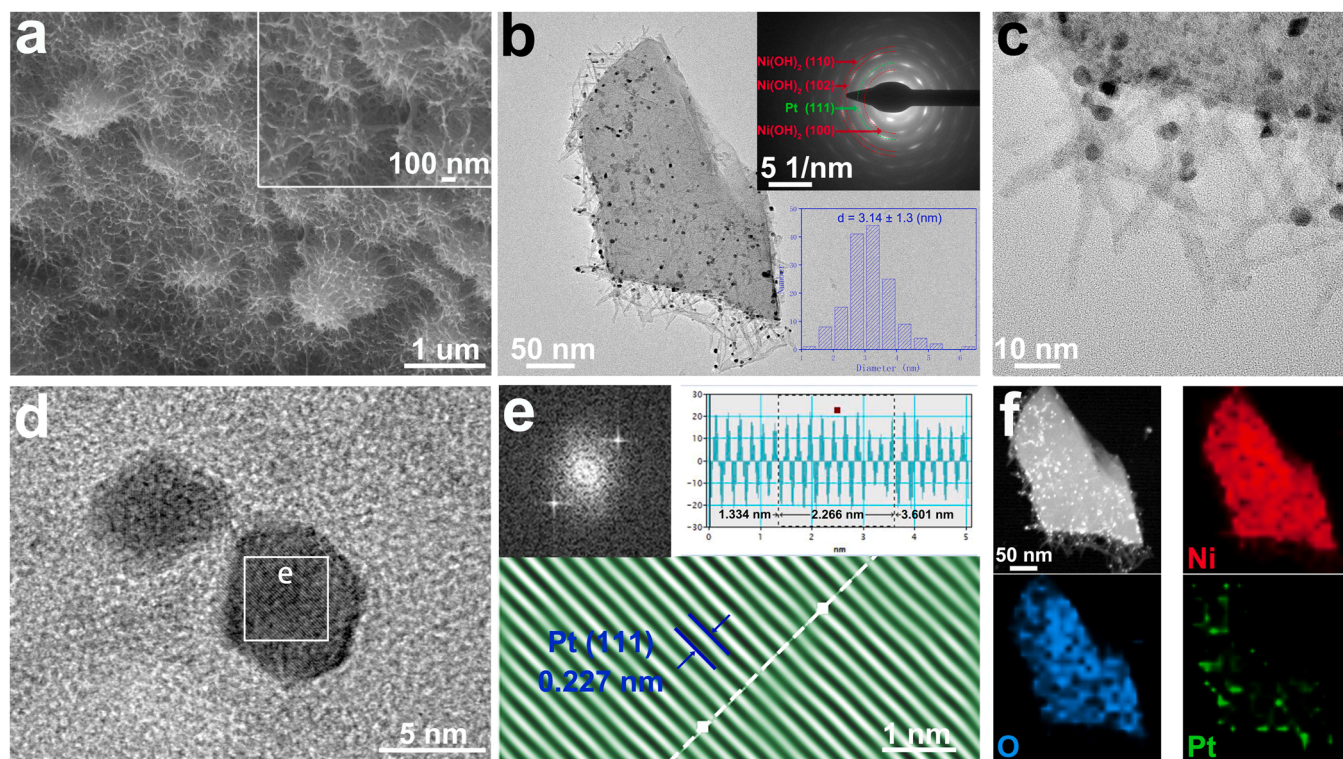


Fig. 3. Pt-Ni(OH)₂@NM: a, SEM image. Inset is the high-magnification image. b, TEM image. Inset is the corresponding SAED pattern and a particle size distribution histogram. c and d, HRTEM images, square area correspond to e, Fast Fourier transformation and inverse Fast Fourier transformation of the selected area. f, EDX elemental mapping images for Ni, O and Pt.

about 8 nm (Fig. S4c), while the nanowires in Pt-Ni(OH)₂ @NM are finer, about 3 nm (Fig. S4f). The internal details of the target sample Pt-Ni(OH)₂ @NM were further observed using TEM (Fig. 3b). Pt nanoparticles with a diameter of approximately 3.14 nm are firmly anchored in the Ni(OH)₂ nanowire/nanosheet composite structure. The SAED diffraction pattern of this region in the inset corresponds to the (100), (102) and (110) planes of Ni(OH)₂, and only two Pt⁰ (111) diffraction spots can be observed. This proves that the crystal orientation of the Pt nanoparticles in this region is homogeneous, which is consistent with the XRD results. To further investigate the state of Pt particles, the nanowire edges were studied using high-resolution TEM (HRTEM). It can be seen that the dark Pt nanoparticles are uniformly dispersed on the light-colored Ni(OH)₂ nanowire/nanosheet region (Fig. 3c), and a further magnified image of these Pt nanoparticles reveals their clear lattice stripes (Fig. 3d). The Fast Fourier transformation and inverse Fast Fourier transformation of the selected region are shown in Fig. 3e, where the 0.227 nm lattice stripe corresponds to Pt⁰ (111). The (111) plane is the low index plane of Pt⁰, which has outstanding stability and catalytic activity [45,46]. The EDS element mapping in Fig. 3f confirms the

uniform distribution of Ni, O and Pt elements in Pt-Ni(OH)₂ @NM. The elemental contents are shown in Fig. S5, and the elemental ratios of Ni(OH)₂ @NM, Pt@NM and Pt-Ni(OH)₂ @NM are shown as a comparison in Table S3. Among them, the detected C and Cu elements were due to the unavoidable errors caused by the carbon film@Cu mesh. Thereafter, the elemental content of Ni(OH)₂ @NM, Pt@NM, and Pt-Ni(OH)₂ @NM was detected by Inductively Coupled Plasma-Atomic Emission Spectrometry (ICP-OES) (Table S4), in which 0.25 cm⁻² of each of the samples were separately dissolved into 1 L solution, respectively. The loading of Pt in Pt-Ni(OH)₂ @NM was determined to be 0.06 mg cm⁻² by combining the above tests.

3.2. HER catalytic performance of samples

A typical three-electrode electrochemical system was assembled to test the HER activity of NF, NM, Ni(OH)₂ @NF, Ni(OH)₂ @NM, Pt@NF, Pt@NM, Pt-Ni(OH)₂ @NF, Pt-Ni(OH)₂ @NM and Pt/C dropped on NM (Pt/C@NM) in alkaline solution (1.0 M KOH). In Fig. 4a and b, the linear scanning voltammetry (LSV) polarization curves show that the HER

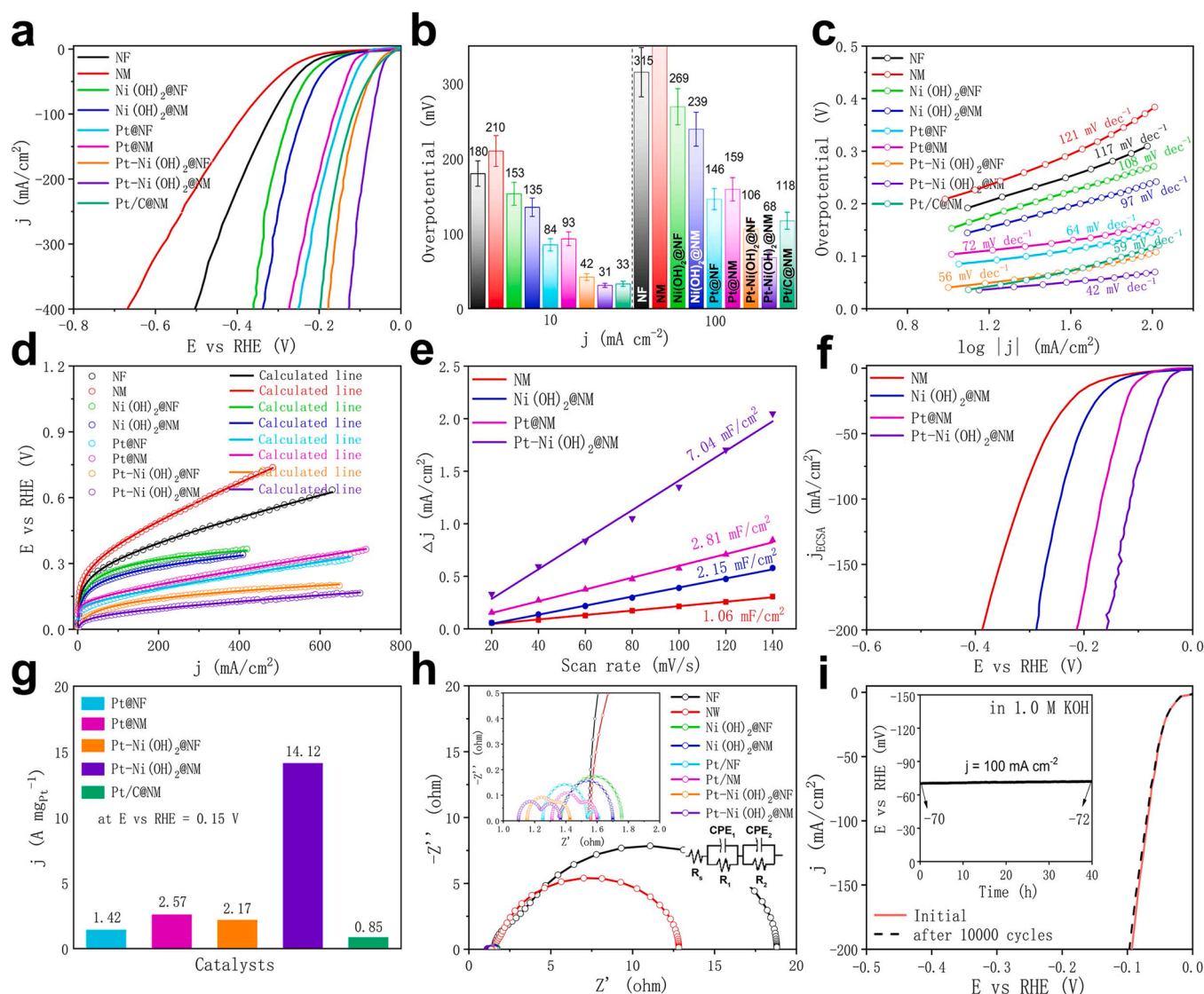


Fig. 4. a-c, HER LSV curves, corresponding overpotentials (at 10, 100 mA cm⁻²) and Tafel slopes for NF, NM, Ni(OH)₂ @NF, Ni(OH)₂ @NM, Pt@NF, Pt@NM, Pt-Ni(OH)₂ @NF, Pt-Ni(OH)₂ @NM and Pt/C@NM tested in 1.0 M KOH. d, LSV curves and calculated plots of catalysts for HER. e, Derived electrical double-layer capacitance (C_{dl}) comparison of NM, Ni(OH)₂ @NM, Pt@NM and Pt-Ni(OH)₂ @NM. f, LSV curves normalized by ECSA. g, Mass activity of the Pt-based catalysts. h, Nyquist plots of the catalysts measured at an overpotential of -50 mV. Inset is the partially enlarged image. i, LSV curves initially and after 10000 CV cycles. Inset is the chronopotentiometry curve of Pt-Ni(OH)₂ @NM at a constant current density of 100 mA cm⁻².

activity is limited for NF ($\eta_{10} = 180$ mV, $\eta_{100} = 315$ mV) and NM ($\eta_{10} = 210$ mV, $\eta_{100} = 376$ mV). After the growth of Ni(OH)_2 , the activities of Ni(OH)_2 @NF ($\eta_{10} = 153$ mV, $\eta_{100} = 269$ mV) and Ni(OH)_2 @NM ($\eta_{10} = 135$ mV, $\eta_{100} = 239$ mV) increases slightly because of the increase in geometric area. Notably, the advantage from the NF substrate (larger geometric area) disappears after the fabrication of Ni(OH)_2 , and the high conductivity of the NM substrate starts to emerge. The enhancement of catalyst performance by the addition of Pt is significant, with the overpotential of both Pt@NF ($\eta_{10} = 85$ mV, $\eta_{100} = 146$ mV) and Pt@NM ($\eta_{10} = 93$ mV, $\eta_{100} = 159$ mV) decreasing to less than half of NF and NM, respectively. As the ideal HER catalyst, Pt can fully leverage its active center. Both Pt-Ni(OH)₂ @NF ($\eta_{10} = 42$ mV, $\eta_{100} = 106$ mV) and Pt-Ni(OH)₂ @NM ($\eta_{10} = 31$ mV, $\eta_{100} = 68$ mV) demonstrated promising HER performance, even surpassing the noble metal catalyst Pt/C@NM ($\eta_{10} = 33$ mV, $\eta_{100} = 117$ mV). Among them, Pt-Ni(OH)₂ @NM exhibited the smallest overpotential, which is inseparable from the dense and homogeneous morphology and dispersed tiny Pt nanoparticles (≈ 3 nm) from TEM images. The Tafel plots calculated from the LSV curve (Fig. 4c) reflect the catalytic kinetics of the HER process. Pt-Ni(OH)₂ @NM (42 mV dec^{-1}) exhibited the smallest Tafel slope compared to the other NF and NM substrate-based catalysts and Pt/C@NM. These data indicate that Pt-Ni(OH)₂ @NM has the smallest HER energy barrier and the fastest reaction kinetics. In addition, the exchange current density (j_0) is positively correlated with the electrochemical reaction rate, which can be obtained by Tafel plot fitting and the Butler-Volmer model [47] (Fig. 4d). Pt-Ni(OH)₂ @NM also showed the maximum j_0 compared with the other catalysts in this work (Table S5). The HER performance of Pt-Ni(OH)₂ @NM remained at an advanced level compared to that of the recently reported noble metal HER catalysts (Table S6).

Furthermore, the non-Faraday interval of the sample was measured using cyclic voltammetry (CV) (Fig. S6), and the double-layer capacitance (C_{dl}) and electrochemical surface area (ECSA) (Fig. 4e) were calculated from the CV results. C_{dl} can be converted into ECSA using the specific capacitance value for a flat standard of 1 cm^2 in the range of $20\text{--}60 \mu\text{F cm}^{-2}$. We assumed it to be $40 \mu\text{F cm}^{-2}$, and the ECSA of Pt-Ni(OH)₂ @NM is about 176 cm^2 . ECSA-normalized specific activity and turnover frequency (TOF) parameters were employed to evaluate the intrinsic activity of the catalyst active sites. From the ECSA-normalized LSV curves of these catalysts (Fig. 4f), it is evident that the active site of Pt-Ni(OH)₂ @NM requires the smallest overpotential to achieve the same current density as NM, Ni(OH)₂ @NM and Pt@NM. TOF of Pt-Ni(OH)₂ @NM was about 21-fold higher than that of NM at an overpotential of 100 mV (Table S7), suggesting the highest efficiency of the active sites on Pt-Ni(OH)₂ @NM during the catalytic process. The above results indicate that the nanowire/nanosheet composite structure of Ni(OH)₂ and minute doping of Pt not only exposes a larger active region but also enhances the intrinsic activity of each active site. These two modulations were combined to achieve the excellent HER activity of Pt-Ni(OH)₂ @NM. To visualize the utilization of Pt, the LSV curves of the Pt-containing catalysts at an overpotential of 150 mV were normalized according to Pt content (Fig. S7). The mass activity of Pt-Ni(OH)₂ @NM is $14.12 \text{ A mg}_{\text{Pt}}^{-1}$, which is 9.94, 5.49, 6.51 and 16.61 times of that of Pt@NF ($1.42 \text{ A mg}_{\text{Pt}}^{-1}$), Pt@NM ($2.57 \text{ A mg}_{\text{Pt}}^{-1}$), Pt-Ni(OH)₂ @NF ($2.17 \text{ A mg}_{\text{Pt}}^{-1}$) and Pt/C@NM ($0.85 \text{ A mg}_{\text{Pt}}^{-1}$), respectively (Fig. 4g). These results indicate that Pt nanoparticles dispersed on Ni(OH)₂ @NM substrates can maximize the HER utilization of Pt, leading to a significant cost reduction. In addition, the charge dynamics of NF, NM, Ni(OH)₂ @NF, Ni(OH)₂ @NM, Pt@NF, Pt@NM, Pt-Ni(OH)₂ @NF and Pt-Ni(OH)₂ @NM were investigated by electrochemical impedance spectroscopy (EIS) (Fig. 4h). Compared to NF ($R_{CT} = 1.55 \Omega$), NM ($R_{CT} = 1.62 \Omega$), Ni(OH)₂ @NF ($R_{CT} = 1.37 \Omega$), Ni(OH)₂ @NM ($R_{CT} = 1.35 \Omega$), Pt@NF ($R_{CT} = 1.27 \Omega$), Pt@NM ($R_{CT} = 1.31 \Omega$) and Pt-Ni(OH)₂ @NF ($R_{CT} = 1.15 \Omega$), Pt-Ni(OH)₂ @NM ($R_{CT} = 1.09 \Omega$) has the smallest charge transfer resistance (R_{CT}), indicating that it offers the least resistance for the electrochemical reaction to occur. In summary, the excellent HER activity of Pt-Ni(OH)₂ @NM was inextricably linked to its large active

region (maximum C_{dl}), high intrinsic activity of the active site (minimum overpotential of LSV normalized by ECSA), and fast charge kinetics (minimum R_{CT}) (Table S7).

Stability is one of the critical determinants for the potential application of a catalyst. After 10000 CV cycles, the LSV curve of Pt-Ni(OH)₂ @NM exhibits only a slight decay (Fig. 4i). The inset shows the chronoamperometric curve of Pt-Ni(OH)₂ @NM for 40 h of continuous operation in 1.0 M KOH at 100 mA cm^{-2} with an increased voltage consumption of only 2.8%. The samples were collected for XRD testing after cycling, Fig. S8a shows that Ni(OH)₂ crystalline features are still evident, and Pt⁰ (111) peak present, except that the samples exhibit certain amorphous features after 30°, and the peak intensities are reduced. The microstructure of Pt-Ni(OH)₂ @NM after the HER cycling test was observed by TEM (Fig. S8b and c), and it was found that no apparent agglomeration occurred in the Ni(OH)₂ nanowire/nanosheet composite structure. In addition, there was no significant change in the dimensions of the anchored Pt particles; a clear lattice stripe with 0.229 nm corresponding to the (111) plane could be detected by HRTEM. The changes in the binding energy of Pt-Ni(OH)₂ @NM after HER cycling were identified by XPS (Fig. S9). The Ni 2p_{3/2} binding energy shifted toward higher values (0.3 eV). In comparison, the Pt 4f_{7/2} binding energy gradually shifted to a lower value (0.2 eV), and the Pt binding energy varied with the adsorption of the adsorbate on the Pt surface. These results indicate a strong interaction between the Ni(OH)₂ and Pt deposited on the surface. To calculate the consumption of Pt-Ni(OH)₂ @NM, 50 mL of electrolyte was collected after the HER cycling test for ICP-OES detection (Table S8). The dissolved Pt content was too low to be detected, and the loss of Ni was $0.0627 \mu\text{g mL}^{-1}$, indicating that the consumption of Pt-Ni(OH)₂ @NM was only 1.3%. This also confirmed the robustness of the Pt particles anchored by the Ni(OH)₂ nanowire/nanosheet composite structures.

3.3. OER and Water splitting performance of samples

Not only did Pt-Ni(OH)₂ @NM show excellent HER activity, but it also exhibited outstanding OER performance in 1.0 M KOH. To avoid the influence of oxidation peak, the overpotentials of 100 and 400 mA cm^{-2} were chosen for the comparison of OER activity. As shown in Fig. 5a and Fig. S10, overpotentials of 382 and 398 mV (η_{100}) are required to reach 100 mA cm^{-2} for pure NF and NM, respectively. Pt-Ni(OH)₂ @NM has the lowest η_{100} (269 mV), which is much smaller than that of Ni(OH)₂ @NF ($\eta_{100} = 387$ mV), Ni(OH)₂ @NM ($\eta_{100} = 359$ mV), Pt@NF ($\eta_{100} = 317$ mV), Pt@NM ($\eta_{100} = 337$ mV), Pt-Ni(OH)₂ @NF ($\eta_{100} = 320$ mV), and the commercial catalyst RuO₂ dropped on NM (RuO₂ @NM) ($\eta_{100} = 298$ mV). This suggests that the larger surface area of the Ni(OH)₂ nanowire/nanosheet composite structure also has a modulating effect on OER activity. Moreover, the catalysts have exhibit higher OER activity after Pt doping; Pt-Ni(OH)₂ @NM shows the smallest Tafel slope (51 mV dec^{-1}) (Fig. 5b) and the largest j_0 (0.072 mA cm^{-2}) (Table S5). The TOF of Pt-Ni(OH)₂ @NM is ≈ 13 -fold higher than NM and ≈ 6 -fold higher than that of Ni(OH)₂ @NM at an overpotential of 300 mV (Table S7). In association with the XPS results, a strong synergistic interaction between the Pt-substrate system guarantees prominent charge transfer and enhances the reaction kinetics of the OER [48]. The OER performance of Pt-Ni(OH)₂ @NM also exceeds that of many reported catalysts in 1.0 M KOH (Table S9).

The Pt-Ni(OH)₂ @NM was then tested for OER cycling (Fig. 5c). LSV curve after 10000 cycles nearly overlapped with the initial curve, and the chronoamperometric curve for 40 h showed a minimal increase in voltage consumption of approximately 2.0%. The Pt-Ni(OH)₂ @NM after OER cycling was characterized by XRD, SEM and TEM (Fig. S11), a significant increase in NiOOH can be seen, demonstrating the generation of Ni oxides/hydroxides in the aqueous and strongly oxidative environment, which is also the active center of OER [49]. The Ni(OH)₂ nanowire/nanosheet composite structure showed little agglomeration after cycling, and the nanosheet structure was exposed in the SEM

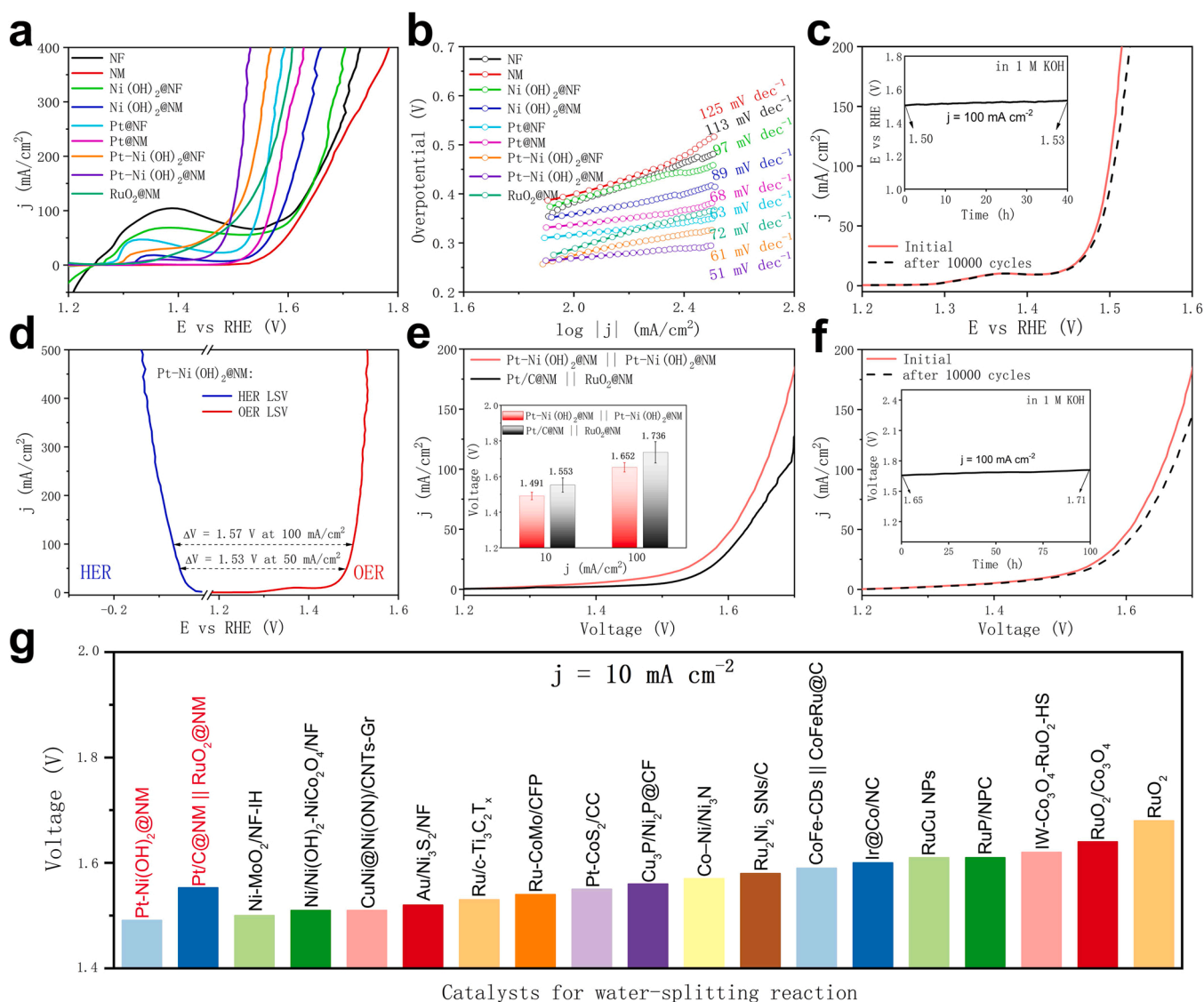


Fig. 5. a, OER LSV curves of NF, NM, Ni(OH)₂@NF, Ni(OH)₂@NM, Pt@NF, Pt@NM, Pt-Ni(OH)₂@NF, Pt-Ni(OH)₂@NM and RuO₂@NM tested in 1.0 M KOH. b, Corresponding Tafel slopes. c, LSV curves initially and after 10000 CV cycles. Inset is the chronopotentiometry curve of Pt-Ni(OH)₂@NM at a constant current density of 100 mA cm⁻². d, LSV curves of Pt-Ni(OH)₂@NM for HER and OER in three-electrode configuration. e, LSV curves of Pt-Ni(OH)₂@NM || Pt-Ni(OH)₂@NM and Pt/C@NM || RuO₂@NM toward overall water splitting in two-electrode configuration. Inset is the corresponding voltages at 10 and 100 mA cm⁻². f, LSV curves initially and after 10000 CV cycles. Inset is the chronopotentiometry curve of Pt-Ni(OH)₂@NM || Pt-Ni(OH)₂@NM at a constant current density of 100 mA cm⁻². g, Comparison with reported catalysts, originating from Table S10.

image. It can be seen from the TEM image that there is an amorphous oxyhydroxide film with a thickness of about 5 nm on the surface of Pt-Ni(OH)₂@NM (Fig. S11c). This oxyhydroxide film not only prevent internal damage but also acts as the active region for the OER under a strong alkaline environment [50]. The excellent OER activity of Pt-Ni(OH)₂@NM cannot be distinguished from the activities of the large number of Ni(OH)₂ nanowire/nanosheet acting as the active center. The changes in the binding energy of Pt-Ni(OH)₂@NM after OER cycling were identified by XPS (Fig. S12). Compared with the initial binding energy, the Ni 2p_{3/2} peak and Pt 4f_{7/2} shift somewhat positively (0.1 eV and 0.2 eV respectively), implying that a transfer of electron density occurs on the surface of Ni-Pt. Moreover, the intensity of Pt⁴⁺ peak is more prominent, corresponding to the change in the binding energy of the strongly oxidizing environment. Moreover, the chemical composition of Ni and Pt were almost unchanged, demonstrating the robust synergistic effect of the Pt-substrate system. These results indicate that Pt-Ni(OH)₂@NM has the potential to be an efficient catalyst for the OER under alkaline conditions.

We also compared the pore size and HER/OER activity of NM with different mesh sizes including 40, 60, 60-thickened, 80, 100 and 200 mesh with pore sizes of 420, 250, 200, 180, 150 and 75 μm respectively (Fig. S13). It is clearly that from 40 mesh NM to 60-thickened mesh NM, both HER and OER activity increased with decreasing pore size. As the pore size continued to decrease, the HER/OER activity dropped sharply (Fig. S14). Thus, 60-thickened mesh NM demonstrated the best HER/OER activity. Moreover, with a thicker nickel wire, there are more active sites, and the cycle life of the catalyst will be more stable. This was the reason for choosing 60-thickened mesh NM as the substrate in this study.

The HER and OER curves in the three-electrode system were combined to form a water-splitting system considering the superior catalytic performance of Pt-Ni(OH)₂@NM in alkaline media. As shown in Fig. 5d, Pt-Ni(OH)₂@NM requires ΔV (ΔV = V_{OER} - V_{HER}) of 1.53 V and 1.57 V to reach 50 and 100 mA cm⁻², respectively. Pt-Ni(OH)₂@NM was assembled into a two-electrode water-splitting system (Pt-Ni(OH)₂@NM || Pt-Ni(OH)₂@NM) and compared to the noble metal electrode Pt/C@NM || RuO₂@NM. The Pt-Ni(OH)₂@NM || Pt-Ni(OH)₂@NM

system requires 1.491 V and 1.652 V to reach 10 and 100 mA cm⁻², respectively, and the hydrolytic activity exceeds that of the Pt/C@NM || RuO₂ @NM combination ($E_{10} = 1.553$ V, $E_{100} = 1.736$ V) (Fig. 5e). The durability of the Pt-Ni(OH)₂ @NM || Pt-Ni(OH)₂ @NM system is shown in Fig. 5f. The LSV curve after 10000 CV cycles exhibits only a small shift compared to the initial LSV curve. The chronoamperometric curve for 100 h shows that the increased voltage consumption at 100 mA cm⁻² is only 3.6%, indicating that the excellent stability of HER and OER is retained in the water-splitting system. In addition, the water-splitting performance of Pt-Ni(OH)₂ @NM || Pt-Ni(OH)₂ @NM is superior to many reported noble-metal-based water-splitting catalysts (Fig. 5g, Table S10). The dissolution of Pt and Ni elements were 0.0652 μg mL⁻¹ and 2.0076 μg mL⁻¹, according to ICP tests, indicating that the consumption of Pt-Ni(OH)₂ @NM || Pt-Ni(OH)₂ @NM was only 4.2% (Table S11). These results demonstrate the excellent water-splitting activity and structural stability of Pt-Ni(OH)₂ @NM || Pt-Ni(OH)₂ @NM system.

3.4. Alkaline water electrolyzer performance of samples

To investigate the effect of catalyst design on the application of alkaline water electrolysis, we designed and assembled an alkaline electrolyzer (Fig. 6a). The gasket was made of PTFE, and the separator (250 μm, AGFA) was a standard part. The device and working process are shown in Fig. S15. Fig. 6b and c are the electrolysis curves for different catalysts. Pt-Ni(OH)₂ @NM shows optimal electrolysis performance, requiring only 1.87 V to reach 400 mA cm⁻² (marked as $E_{0.4A}$) at 80 °C (simulation of actual working conditions) and only 2.24 V to reach 1000 mA cm⁻² (marked as E_{1A}) at 80 °C. In comparison, NM needs the largest voltage ($E_{0.4A} = 2.47$ V, $E_{1A} = 3.13$ V) and the Pt/C@NM-RuO₂ @NM combination also exhibits poor performance ($E_{0.4A} = 2.16$ V, $E_{1A} = 2.78$ V), probably due to the low utilization of noble metals and the loose bonding of catalyst powder between substrate. In contrast, Pt-Ni

(OH)₂ @NF has a slightly inferior performance ($E_{0.4A} = 2.02$ V, $E_{1A} = 2.51$ V) than Pt-Ni(OH)₂ @NM, probably due to the larger R_{CT} . To further investigate the water electrolysis performance of the different catalysts, their voltage compositions were analyzed. The total overpotential (η_{Total}) was divided into the ohmic overpotential (η_{Ohm}) and kinetic overpotential (η_{kin}), corresponding to the electrolytic voltage (E_{Cell}), IR-corrected voltage ($E_{IR-corrected}$), and kinetic voltage (E_{kin}) (Fig. S16). η_{Ohm} is caused by the resistance between the components in the system and cannot be entirely avoided. The maximum possible simplification of the components and optimization of the system design are the most effective ways to reduce η_{Ohm} . Although η_{kin} is mainly determined by the catalyst, the smallest η_{kin} of Pt-Ni(OH)₂ @NM indicates the best catalytic activity. The efficient maintenance of the balance between the cost and voltage consumption is key to the application.

Fig. 6d demonstrates that the material cost of 9 cm² Pt-Ni(OH)₂ @NM assembled in the electrolyzer increases by only 0.12 ¥ or 0.002 \$ cm⁻² relative to pure NM, whereas the voltage required to reach 1 A cm⁻² is reduced by 0.89 V. The voltage efficiency (E_{the} (theoretical water electrolysis) / E_{onset} (actual voltage at 1 mA cm⁻²)) improves from 83.10% (NM) to 91.04% (Pt-Ni(OH)₂ @NM) (Fig. S17). The positive effect of Pt-Ni(OH)₂ @NM in the alkaline electrolyzer was also confirmed by the EIS results. Fig. 6e shows that the ohmic impedance of Pt-Ni(OH)₂ @NM decreases by 50.4%, 23.1% and 27.4% when compared to NM, Pt-Ni(OH)₂ @NF and Pt/C@NM-RuO₂ @NM at 1.60 V, respectively. Furthermore, the stability test demonstrated that the Pt-Ni(OH)₂ @NM can work steadily for 600 h at 80 °C and 400 mA cm⁻², with a voltage decay rate of only 0.13 mV h⁻¹ (Fig. 6f). However, the Pt-Ni(OH)₂ @NF exhibited a significant voltage decay rate of 2.44 mV h⁻¹ before 180 h of operation. The post-cycling SEM and TEM images showed the dramatic destruction of the Ni(OH)₂ nanowire/nanosheet composite structure of Pt-Ni(OH)₂ @NF, and the Pt nanoparticles were also heavily agglomerated due to the loss of anchoring

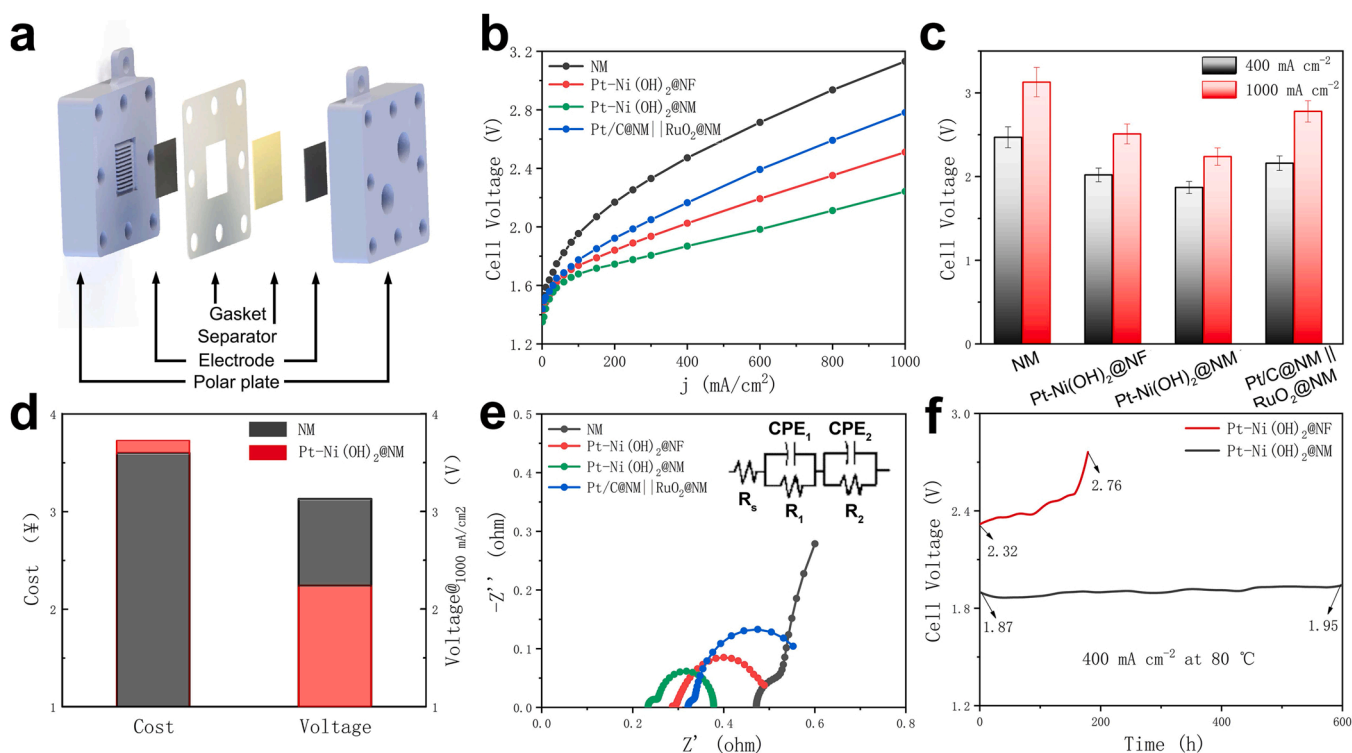


Fig. 6. a, Schematic of alkaline water electrolyzer. b, LSV curves of NM, Pt-Ni(OH)₂ @NF, Pt-Ni(OH)₂ @NM and Pt/C@NM || RuO₂ @NM at 80 °C in 1 M KOH. c, The overvoltage of alkaline electrolyzers at 400 mA cm⁻² and 1000 mA cm⁻². d, Comparison of cost and voltage consumption between NM and Pt-Ni(OH)₂ @NM electrodes (9 cm²). e, Nyquist plots at E_{cell} of 1.60 V. Inset is the equivalent circuit diagram. f, Time-dependent voltage curves for Pt-Ni(OH)₂ @NF and Pt-Ni(OH)₂ @NM at 400 mA cm⁻² for 600 h.

(Fig. S18), leading to a sharp deterioration of water electrolysis. In contrast, the Ni(OH)₂ structure of Pt-Ni(OH)₂ @NM remained intact with only partial agglomeration (Fig. S19), thus enabling stable operation for more than 600 h. This finding demonstrates the advantage of the NM substrate with high mechanical strength.

Thus, the high catalytic activity and stability of Pt-Ni(OH)₂ @NM discussed in this work can be attributed to the following: (1) The dense and homogeneous nanowire/nanosheet composite structure provides a larger surface area and more exposed active sites. (2) Pt doping modulates the electronic binding energy of the catalyst. (3) Higher intrinsic activity, larger ECSA and smaller R_{CT} effectively reduce the energy barrier for the catalytic reaction. (4) The in situ growth of Ni(OH)₂ nanostructures on NM substrates and electrochemically doped Pt⁰ lead to tight bonding, thus ensuring efficient charge transfer and long-term operational stability.

4. Conclusion

In summary, an extremely low Pt-content Ni(OH)₂ nanowire/nanosheet composite array based on an NM substrate was designed as an electrode to achieve excellent HER, OER and water electrolysis in alkaline electrolyte. The ECSA and charge transfer rate were enhanced by the construction of Ni(OH)₂ and appropriate Pt doping to regulate the electronic binding energy, which reduced the energy barrier required for the catalytic reaction. Consequently, the electrode exhibited outstanding catalytic activity (only 68 mV and 269 mV overpotential were required to reach 100 mA cm⁻² for HER and OER in alkaline electrolytes, respectively), which outperform the noble metal catalysts Pt/C@NM and RuO₂ @NM. Notably, the material cost of the electrode only increases by 0.002 \$ cm⁻² with a superior water electrolysis performance (1.87 V @ 400 mA cm⁻², 2.24 V @ 1000 mA cm⁻² and can work steadily for more than 600 h). Thus, this work not only presents a design concept for low-cost electrodes with outstanding performance but also assembles them into an alkaline water electrolyzer for actual water electrolysis, which has the potential for real application.

CRediT authorship contribution statement

Junyu Zhang: Conceptualization, Writing – original draft, Writing – review & editing, Formal analysis. **Jian Dang:** Methodology, Validation, Software, Formal analysis, Writing – review & editing. **Xiaohong Zhu:** Methodology, Investigation, Resources. **Jugang Ma:** Methodology, Investigation, Writing – review & editing. **Minggao Ouyang:** Supervision, Project administration. **Fuyuan Yang:** Supervision, Project administration, Funding acquisition.

Declaration of Competing Interest

The authors declare that they have no known competing financial interests or personal relationships that could have appeared to influence the work reported in this paper.

Data Availability

No data was used for the research described in the article.

Appendix A. Supporting information

Supplementary data associated with this article can be found in the online version at doi:10.1016/j.apcatb.2022.122296. Additional details of formula derivation and analysis, XRD patterns, SEM images, TEM images, electrochemical characterizations and comparative data.

References

- [1] M. De Rosa, K. Gainsford, F. Pallonetto, D.P. Finn, Diversification, concentration and renewability of the energy supply in the European Union, *Energy* 253 (2022), 124097.
- [2] S. Ren, P. Wang, Z. Lin, D. Zhao, The policy choice and economic assessment of high emissions industries to achieve the carbon peak target under energy shortage—a case study of Guangdong Province, *Energies* 15 (2022) 6750.
- [3] X. Zhang, B. Wang, S. Zhao, H. Li, H. Yu, Oxygen anionic redox activated high-energy cathodes: status and prospects, *eTransportation* 8 (2021), 100118.
- [4] Y. Chen, D. Xia, Systematic density functional theory investigations on cubic lithium-rich iron-based Li₂FeO₃: a multiple electrons cationic and anionic redox cathode material, *eTransportation* 10 (2021), 100141.
- [5] T. Liu, X.-G. Yang, S. Ge, Y. Leng, C.-Y. Wang, Ultrafast charging of energy-dense lithium-ion batteries for urban air mobility, *eTransportation* 7 (2021), 100103.
- [6] X. Feng, Y. Merla, C. Weng, M. Ouyang, X. He, B.Y. Liaw, S. Santhanagopalan, X. Li, P. Liu, L. Lu, X. Han, D. Ren, Y. Wang, R. Li, C. Jin, P. Huang, M. Yi, L. Wang, Y. Zhao, Y. Patel, G. Offer, A reliable approach of differentiating discrete sampled-data for battery diagnosis, *eTransportation* 3 (2020), 100051.
- [7] G. Liu, J. Xu, T. Chen, K. Wang, Progress in thermoplasmonics for solar energy applications, *Phys. Rep.* 981 (2022) 1–50.
- [8] J. Liang, M. Irfan, M. Ikram, D. Zimon, Evaluating natural resources volatility in an emerging economy: the influence of solar energy development barriers, *Resour. Policy* 78 (2022), 102858.
- [9] N. Zhang, J. Zheng, G. Song, H. Zhao, Regional comprehensive environmental impact assessment of renewable energy system in California, *J. Clean. Prod.* 376 (2022), 134349.
- [10] H. Ishaq, I. Dincer, C. Crawford, A review on hydrogen production and utilization: challenges and opportunities, *Int. J. Hydrog. Energy* 47 (2022) 26238–26264.
- [11] B.E. Lebrunhi, J.J. Djoupo, B. Lamrani, K. Benabdelaziz, T. Kousksou, Global hydrogen development - a technological and geopolitical overview, *Int. J. Hydrog. Energy* 47 (2022) 7016–7048.
- [12] T. Wang, L. Tao, X. Zhu, C. Chen, W. Chen, S. Du, Y. Zhou, B. Zhou, D. Wang, C. Xie, P. Long, W. Li, Y. Wang, R. Chen, Y. Zou, X.-Z. Fu, Y. Li, X. Duan, S. Wang, Combined anodic and cathodic hydrogen production from aldehyde oxidation and hydrogen evolution reaction, *Nature, Catalysis* 5 (2021) 66–73.
- [13] International Energy Agency, Net Zero by 2050 A Roadmap for the Global Energy Sector, (2021) 1–222.
- [14] B.A. Pinaud, J.D. Benck, L.C. Seitz, A.J. Forman, Z. Chen, T.G. Deutsch, B.D. James, K.N. Baum, G.N. Baum, S. Ardo, H. Wang, E. Miller, T.F. Jaramillo, Technical and economic feasibility of centralized facilities for solar hydrogen production via photocatalysis and photoelectrochemistry, *Energy Environ. Sci.* 6 (2013) 1983–2002.
- [15] International Renewable Energy Agency, Green Hydrogen Cost Reduction: Scaling up Electrolysers to Meet the 1.5 °C Climate Goal, (2020) 1–103.
- [16] Z.P. Cano, D. Banham, S. Ye, A. Hintennach, J. Lu, M. Fowler, Z. Chen, Batteries and fuel cells for emerging electric vehicle markets, *Nature, Energy* 3 (2018) 279–289.
- [17] M. Qiao, Y. Wang, Q. Wang, G. Hu, X. Mamat, S. Zhang, S. Wang, Hierarchically ordered porous carbon with atomically dispersed FeN₄ for ultraefficient oxygen reduction reaction in proton-exchange membrane fuel cells, *Angew. Chem. Int. Ed.* 59 (2020) 2688–2694.
- [18] M. Jin, X. Zhang, S. Niu, Q. Wang, R. Huang, R. Ling, J. Huang, R. Shi, A. Amini, C. Cheng, Strategies for designing high-performance hydrogen evolution reaction electrocatalysts at large current densities above 1000 mA cm⁻², *ACS Nano* (2022) 11577–11597.
- [19] X. Xie, L. Du, L. Yan, S. Park, Y. Qiu, J. Sokolowski, W. Wang, Y. Shao, Oxygen evolution reaction in alkaline environment: material challenges and solutions, *Adv. Funct. Mater.* 32 (2022) 2110036.
- [20] Q. Wen, Y. Zhao, Y. Liu, H. Li, T. Zhai, Ultrahigh-current-density and long-term-durability electrocatalysts for water splitting, *Small* 18 (2022) e2104513.
- [21] Z. Kou, K. Wang, Z. Liu, L. Zeng, Z. Li, B. Yang, L. Lei, C. Yuan, Y. Hou, Recent advances in manifold exfoliated synthesis of two-dimensional non-precious metal-based nanosheet electrocatalysts for water splitting, *Small Struct.* 3 (2021) 2100153.
- [22] Z. Wei, T. Liu, L. Zhang, J. Yu, Sulfide-based nickel-plated fabrics for foldable Quasi-solid-state supercapacitors, *Energy Environ. Mater.* 5 (2021) 883–891.
- [23] H. Zhou, H. Wang, C. Lai, Z. Guo, J. Hu, S. Ji, L. Lei, Hierarchical heterogeneous NiFe-LDH/Ni/NM nanosheets grown in situ for stably overall water splitting at large current densities, *J. Electroanal. Chem.* 919 (2022), 116527.
- [24] N.S. Gultom, H. Abdullah, C.-N. Hsu, D.-H. Kuo, Activating nickel iron layer double hydroxide for alkaline hydrogen evolution reaction and overall water splitting by electrodepositing nickel hydroxide, *Chem. Eng. J.* 419 (2021), 129608.
- [25] D. Li, X. Chen, Y. Lv, G. Zhang, Y. Huang, W. Liu, Y. Li, R. Chen, C. Nuckolls, H. Ni, An effective hybrid electrocatalyst for the alkaline HER: highly dispersed Pt sites immobilized by a functionalized NiRu-hydroxide, *Appl. Catal. B: Environ.* 269 (2020), 118824.
- [26] Y. Wu, S. Ji, H. Wang, B.G. Pollet, X. Wang, R. Wang, A highly efficient water electrolyser cell assembled by asymmetric array electrodes based on Co, Fe-doped Ni(OH)₂ nanosheets, *Appl. Surf. Sci.* 528 (2020), 146972.
- [27] Y. Zhao, Y. Gao, Z. Chen, Z. Li, T. Ma, Z. Wu, L. Wang, Trifluoromethyl Pt coupled with NiFe hydroxide synthesized via corrosion engineering to boost the cleavage of water molecule for alkaline water-splitting, *Appl. Catal. B: Environ.* 297 (2021), 120395.
- [28] X. Han, X. Wu, Y. Deng, J. Liu, J. Lu, C. Zhong, W. Hu, Ultrafine Pt nanoparticle-decorated pyrite-type CoS₂ nanosheet arrays coated on carbon cloth as a

- bifunctional electrode for overall water splitting, *Adv. Energy Mater.* 8 (2018) 1800935.
- [29] J.-Y. Zhang, Y. Yan, B. Mei, R. Qi, T. He, Z. Wang, W. Fang, S. Zaman, Y. Su, S. Ding, B.Y. Xia, Local spin-state tuning of cobalt-iron selenide nanoframes for the boosted oxygen evolution, *Energy Environ. Sci.* 14 (2021) 365–373.
- [30] Y. Wang, X. Li, M. Zhang, Y. Zhou, D. Rao, C. Zhong, J. Zhang, X. Han, W. Hu, Y. Zhang, K. Zaghib, Y. Wang, Y. Deng, Lattice-strain engineering of homogeneous $\text{NiS}_{0.5}\text{Se}_{0.5}$ core-shell nanostructure as a highly efficient and robust electrocatalyst for overall water splitting, *Adv. Mater.* 32 (2020) e2000231.
- [31] Y. Wang, X. Li, M. Zhang, J. Zhang, Z. Chen, X. Zheng, Z. Tian, N. Zhao, X. Han, K. Zaghib, Y. Wang, Y. Deng, W. Hu, Highly active and durable single-atom tungsten-doped $\text{NiS}_{0.5}\text{Se}_{0.5}$ Nanosheet @ $\text{NiS}_{0.5}\text{Se}_{0.5}$ nanorod heterostructures for water splitting, *Adv. Mater.* 34 (2022), e2107053.
- [32] X. Gao, W. Zang, X. Li, Z. Wang, L. Zheng, Z. Kou, Achieving efficient alkaline hydrogen evolution reaction on long-range Ni sites in Ru clusters-immobilized Ni_3N array catalyst, *Chem. Eng. J.* 451 (2023), 138698.
- [33] C.G. Morales-Guio, L.A. Stern, X. Hu, Nanostructured hydrotreating catalysts for electrochemical hydrogen evolution, *Chem. Soc. Rev.* 43 (2014) 6555–6569.
- [34] A. Nairan, C. Liang, S.-W. Chiang, Y. Wu, P. Zou, U. Khan, W. Liu, F. Kang, S. Guo, J. Wu, C. Yang, Proton selective adsorption on Pt–Ni nano-thorn array electrodes for superior hydrogen evolution activity, *Energy Environ. Sci.* 14 (2021) 1594–1601.
- [35] K.L. Zhou, Z. Wang, C.B. Han, X. Ke, C. Wang, Y. Jin, Q. Zhang, J. Liu, H. Wang, H. Yan, Platinum single-atom catalyst coupled with transition metal/metal oxide heterostructure for accelerating alkaline hydrogen evolution reaction, *Nat. Commun.* 12 (2021) 3783.
- [36] S. Tao, Q. Wen, W. Jaegermann, B. Kaiser, Formation of highly active $\text{NiO}(\text{OH})$ thin films from electrochemically deposited $\text{Ni}(\text{OH})_2$ by a simple thermal treatment at a moderate temperature: a combined electrochemical and surface science investigation, *ACS, ACS Catal.* 12 (2022) 1508–1519.
- [37] W.D. Yang, R.D. Zhao, J. Xiang, S. Loy, Y.F. Di, J. Li, M.T. Li, D.M. Ma, F.F. Wu, 3D hierarchical $\text{ZnCo}_2\text{S}_4/\text{Ni}(\text{OH})_2$ nanowire arrays with excellent flexible energy storage and electrocatalytic performance, *J. Colloid Interface Sci.* 626 (2022) 866–878.
- [38] J. Zhang, S. Wei, Y. Liu, G. Wang, Y. Cui, A. Dong, S. Xu, J. Lian, Q. Jiang, Invigorating the catalytic performance of CoP through interfacial engineering by Ni_2P precipitation, *J. Mater. Chem. A* 7 (2019) 26177–26186.
- [39] J. Zhang, J. Lian, Q. Jiang, G. Wang, Boosting the OER/ORR/HER activity of Ru-doped Ni/Co oxides heterostructure, *Chem. Eng. J.* 439 (2022), 135634.
- [40] K.L. Zhou, C. Wang, Z. Wang, C.B. Han, Q. Zhang, X. Ke, J. Liu, H. Wang, Seamlessly conductive $\text{Co}(\text{OH})_2$ tailored atomically dispersed Pt electrocatalyst with a hierarchical nanostructure for an efficient hydrogen evolution reaction, *Energy Environ. Sci.* 13 (2020) 3082–3092.
- [41] C.D. Wagner, Chemical shifts of Auger lines, and the Auger parameter, *Faraday Discuss. Chem. Soc.* 60 (1975) 291–300.
- [42] J.D. Rogers, V.S. Sundaram, G.G. Kleiman, S.G.C. Castro, R.A. Douglas, A. C. Peterlevitz, High resolution study of the $\text{M}_{45}\text{N}_{67}\text{N}_{67}$ and $\text{M}_{45}\text{N}_{45}\text{N}_{67}$ Auger transitions in the 5d series, *J. Phys. F Met. Phys.* 12 (1982) 2097.
- [43] S. Ye, F. Luo, Q. Zhang, P. Zhang, T. Xu, Q. Wang, D. He, L. Guo, Y. Zhang, C. He, X. Ouyang, M. Gu, J. Liu, X. Sun, Highly stable single Pt atomic sites anchored on aniline-stacked graphene for hydrogen evolution reaction, *Energy Environ. Sci.* 12 (2019) 1000–1007.
- [44] W. Zhong, B. Xiao, Z. Lin, Z. Wang, L. Huang, S. Shen, Q. Zhang, L. Gu, RhSe_2 : a superior 3D electrocatalyst with multiple active facets for hydrogen evolution reaction in both acid and alkaline solutions, *Adv. Mater.* 33 (2021), e2007894.
- [45] N.M. Marković, H.A. Gasteiger, P.N.J. Ross, Oxygen reduction on platinum low-index single-crystal surfaces in sulfuric acid solution: rotating ring-Pt(*hkl*) disk studies, *J. Phys. Chem.* 99 (1995) 3411–3415.
- [46] M. Xie, Z. Lyu, R. Chen, M. Shen, Z. Cao, Y. Xia, Pt-Co@Pt octahedral nanocrystals: enhancing their activity and durability toward oxygen reduction with an intermetallic core and an ultrathin shell, *J. Am. Chem. Soc.* 143 (2021) 8509–8518.
- [47] M. Espinosa-López, C. Darras, P. Poggi, R. Glises, P. Baucour, A. Rakotondrainibe, S. Besse, P. Serre-Combe, Modelling and experimental validation of a 46 kW PEM high pressure water electrolyzer, *Renew. Energy* 119 (2018) 160–173.
- [48] Y. Chen, H. Yao, F. Kong, H. Tian, G. Meng, S. Wang, X. Mao, X. Cui, X. Hou, J. Shi, V_2C MXene synergistically coupling FeNi LDH nanosheets for boosting oxygen evolution reaction, *Appl. Catal. B: Environ.* 297 (2021), 120474.
- [49] S. Jin, Are metal chalcogenides, nitrides, and phosphides oxygen evolution catalysts or bifunctional catalysts? *ACS Energy Lett.* 2 (2017) 1937–1938.
- [50] S. Lee, A. Moysiadou, Y.-C. Chu, H.M. Chen, X. Hu, Tracking high-valent surface iron species in the oxygen evolution reaction on cobalt iron (oxy)hydroxides, *Energy Environ. Sci.* 15 (2022) 206–214.